Journal of Materials Chemistry C

ROYAL SOCIETY OF CHEMISTRY

PAPER

View Article Online
View Journal | View Issue

Cite this: J. Mater. Chem. C, 2024, 12, 6098

Homochirality to design high-T_c lead-free ferroelastic semiconductors†

Bo-Wen Deng,[a] Zhi-Peng Rao,[a] Ming-Jing Shen,[a] Ke-Wei Liang,[c] Yang Zhu,[a] Zhi-Jie Wang,[a] Kun Ding,[a] Chang-Yuan Su,[a] Meng-Meng Lun,[a] Zhi-Xu Zhang,*[a] Yi Zhang*[b] and Da-Wei Fu*[b]

Received 30th January 2024,
Accepted 1st April 2024

DOI: 10.1039/d4tc00428k

rsc.li/materials-c

Ferroelastic semiconductor materials have garnered significant research interest due to their promising applications in the fields of shape memory, superelasticity, templated electronic nanostructures, mechanical switching, and optoelectronic transmission. However, the toxicity of lead-based structures and low phase-transition temperature (T_c) greatly constrain the application scenarios of ferroelastic semiconductors. Here, using an H/OH-substitution-induced homochiral strategy, we synthesize a pair of lead-free ferroelastic semiconductors (*R*/*S*-CTA)$_2$SbCl$_5$ (CTA = 3-chloro-2-hydroxypropyltrimethyllammonium) having semiconductor properties with an indirect bandgap of 3.41 eV. They crystallized in the chiral space group $P2_12_12_1$ at room temperature, and both undergo 422F222 type ferroelastic phase transitions with T_c up to 410 K, accompanied by a large entropy change of 68.75 and 66.09 J mol^{-1} K^{-1}, respectively. Owing to the introduction of chirality, they exhibited temperature-dependent nonlinear second-harmonic generation (SHG) properties. Relatively, the achiral TMCP (TMCP = *N*,*N*,*N*-trimethylchloropropylamine) makes the phase transition properties of centrosymmetric TMCP$_2$SbCl$_5$ ordinary compared to chiral *R*/*S*-pair. This is precisely the main starting point of homochiral strategies in phase transition and optical structure research, while arousing research interest. This work, which provides a new avenue for the design of high-T_c lead-free ferroelastic semiconductor compounds, is a powerful motivation for the realization of multifunctional materials related to chirality.

Introduction

Organic–inorganic hybrid perovskites have been the focus of research in the fields of chips, photovoltaics, and batteries due to their good mechanical reversibility, long carrier transport distance, and high structural flexibility.[1–18] Recently, the ferroelasticity of the popular hybrid semiconductor $CH_3NH_3PbI_3$ has been demonstrated to be beneficial for the improvement of photovoltaic efficiency,[19] while the ferroelastic domain wall facilitates benign carrier transport, thus giving rise to extensive research on ferroelastic semiconductors.[20–22] However, most of the reported ferroelastic semiconductors are lead halide-based structures, where heavy metals are toxic and can cause great harm to organisms and the environment.[23–27] Organic–inorganic hybrid perovskite semiconductor structures have structural diversity and tunability, and metallic lead can usually be replaced by non-toxic metallic elements such as Ge(II), Sn(II), Bi(III), and Sb(III).[28–30] Therefore, some lead-free semiconductors have been constructed by this method, such as dimethylamineGeI$_3$,[31] [*R*-3-hydroxylpiperidinium]$_2$SbCl$_5$,[32] and (3-bromopropylaminium)$_4$AgBiBr$_8$.[33] In addition, the low phase transition temperatures in these hybrid perovskites ferroelastic semiconductors limit their further applications at high temperatures and in special environments.[34–39] Hence, it is imperative to advance the development of lead-free ferroelastic semiconductors with high phase transition temperatures.

Halogen substitution,[25,26,39] mixed cation engineering,[40] and the introduction of homochirality[23,26,32,41,42] are commonly used to regulate ferroelastic materials in organic–inorganic hybrid systems. The incorporation of homochirality is advantageous for achieving a multi-channel bistable response in ferroelastic materials, garnering widespread research and attention. Luo and his coworkers introduced homochirality into (*Rac*-3-OHpyl)PbBr$_3$ (OHpyl = hydroxypyrrolium), achieving a pair of eight channel bistable response of chiral ferroelastic compound (*R*/*S*-3-OHpyl)PbBr$_3$ with dielectric, DSC,

[a] Ordered Matter Science Research Center, Jiangsu Key Laboratory for Science and Applications of Molecular Ferroelectrics, Southeast University, Nanjing 211189, People's Republic of China. E-mail: zhangzhixu@zjnu.edu.cn
[b] Institute for Science and Applications of Molecular Ferroelectrics, Key Laboratory of the Ministry of Education for Advanced Catalysis Materials, Zhejiang Normal University, Jinhua, People's Republic of China. E-mail: dawei@zjnu.edu.cn, yizhang1980@seu.edu.cn
[c] School of Electronic and Communication Engineering, Tianjin Normal University, Tianjin 300387, People's Republic of China

† Electronic supplementary information (ESI) available: Experimental details, Fig. S1–S9 and Tables S1–S6. CCDC 2324820–2324822 and 2343331. For ESI and crystallographic data in CIF or other electronic format see DOI: https://doi.org/10.1039/d4tc00428k

SHG, ferroelasticity, conductivity, photoluminescence, circular dichroism, and photocurrent response.[43] Xiong's group reported a thermochromic ferroelastic compound $(R/S\text{-CTA})_2CuCl_4$ with seven physical channels.[44] The introduction of homochirality can be used to precisely design ferroelastic materials with multi-channel switches, but it does have certain limitations in obtaining ferroelastic materials with high-T_c. Therefore, we use the H/OH-substitution-induced homochiral strategy to achieve the construction of high-T_c ferroelastic semiconductors. On the one hand, the introduction of hydroxyl groups induces hydrogen bonding, which increases the potential energy barrier for cation motion to raise the T_c.[36,45] On the other hand, the introduction of chiral cations alters the microstructure of the crystals, allowing the construction of ferroelasticity, and also enables the compounds to crystallize in non-centrosymmetric space groups, enabling the molecules to be SHG-responsive.[41,42,44,46,47]

Based on the homochiral strategy, we have successfully synthesized high-T_c lead-free ferroelastic semiconductor compounds $(R\text{-CTA})_2SbCl_5$ and $(S\text{-CTA})_2SbCl_5$ (CTA = 3-chloro-2-hydroxypropyltrimethyllammonium). $(R\text{-CTA})_2SbCl_5$ and $(S\text{-CTA})_2SbCl_5$ undergo a plastic phase transition at 410 K, having a large entropy change of 68.75 and 66.09 J mol^{-1} K^{-1}, respectively. Compared to $TMCP_2SbCl_5$ (TMCP = *N*,*N*,*N*-trimethylchloropropylamine), the introduction of hydroxyl groups increases the T_c of $(R/S\text{-CTA})_2SbCl_5$ by 20 K, and the introduction of chirality allows $(R/S\text{-CTA})_2SbCl_5$ to crystallize in non-centrosymmetric space groups, accompanied by switchable second-harmonic generation (SHG) between SHG-active and SHG-inactive states. A comparison of variable-temperature PXRD and SHG results reveals that $(R/S\text{-CTA})_2SbCl_5$ undergoes the 422F222 type ferroelastic phase transition and possesses excellent temperature dependence and reversibility. This work has successfully obtained high-T_c lead-free ferroelastic semiconductor compounds using the strategy of H/OH-substitution-induced homochirality (Scheme 1), while injecting fresh energy into the realization of chiral related multifunctional materials.

Results and discussion

Crystal structure analysis

In order to explore the details and microscopic mechanisms of the crystal structure, we used X-ray diffraction to measure the crystallographic data of $TMCP_2SbCl_5$ and $(R/S\text{-CTA})_2SbCl_5$. At 293 K, $TMCP_2SbCl_5$ crystallizes in the monoclinic central space group $P2_1/c$, with unit cell parameters of a = 8.5967(4) Å, b = 31.8060(15) Å, c = 9.6375(5) Å, β = 115.487°, V = 2378.7(2) Å^3, and Z = 4. The inorganic skeleton and the cations exhibit an ordered state (Fig. S4a, ESI†). The inorganic skeleton is connected to 5 Cl atoms with Sb atoms as the center, presenting a pyramid configuration. The Sb–Cl bond length and Cl–Sb–Cl bond angle range from 2.3680(14) to 2.6774(12) and from 87.83(7) to 177.62(5), respectively (Table S3, ESI†). The inorganic skeleton and organic cations alternate to form a zero-dimensional packing structure (Fig. 1a). The introduction of chirality often brings about structural changes, thereby inducing some novel properties. Here we use hydroxyl group substitution to induce homochirality, allowing $(R/S\text{-CTA})_2SbCl_5$ to crystallize in the chiral space group, which not only induces SHG signals but also enables ferroelastic phase transitions. $(R/S\text{-CTA})_2SbCl_5$ crystallizes in the space group $P2_12_12_1$, with unit cell parameters of a = 8.9032(3) Å, b = 9.5971(3) Å, c = 28.2922(8) Å, V = 2417.42(12) Å^3, Z = 4 and a = 8.9021(2) Å, b = 9.5969(2) Å, c = 28.2865(7) Å, V = 2416.59(10) Å^3, Z = 4 at 293 K, respectively. The smallest independent unit consists of two CTA cations and one $[SbCl_5]^{2-}$ anion skeleton (Fig. S4b and c, ESI†), with the organic part exhibiting an ordered state. The inorganic skeleton in $(S\text{-CTA})_2SbCl_5$ is similar to that in $TMCP_2SbCl_5$, with the Sb–Cl bond length and Cl–Sb–Cl bond angle ranging from 2.3606(10) to 2.6993(12) and 87.46(4) to 176.62(4), respectively (Table S1, ESI†). $(R/S\text{-CTA})_2SbCl_5$ exhibits a zero-dimensional packing form, and possesses a mirror symmetry relationship (Fig. 1b). In Fig. 1d, there is an O–H···Cl interaction force between the cation and the anion in $(R\text{-CTA})_2SbCl_5$, and the stretching leads to a longer Sb–Cl4 bond. In contrast, there is no hydrogen bonding interaction in $TMCP_2SbCl_5$, so the bond length of Sb–Cl4 in $TMCP_2SbCl_5$ is smaller than that of Sb–Cl4 in $(R\text{-CTA})_2SbCl_5$ (Fig. 1c and d).

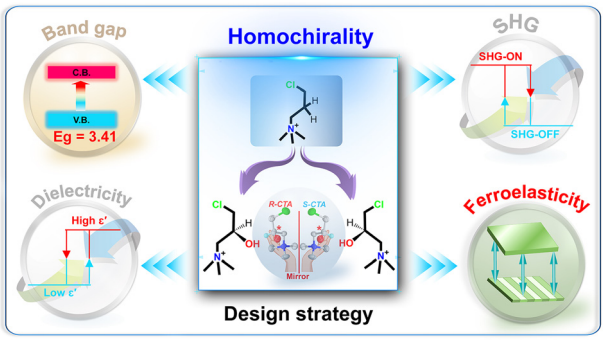

Scheme 1 Schematic diagram of the molecular design strategy for constructing high-T_c lead-free ferroelastic semiconductors.

Intermolecular interaction analysis

To further illustrate that $(S/R\text{-CTA})_2SbCl_5$ has relatively stronger intermolecular internal forces compared to $TMCP_2SbCl_5$, the CrystalExplorer software was used to calculate and evaluate the Hirshfeld d_{norm} surfaces, and two-dimensional fingerprints of cations were plotted. The results show that the short contact (red concave area on the surface) between *R*/*S*-CTA cations is more compact than that of TMCP cations (Fig. 2a–c). At the same time, from Fig. 2d–f, it can be seen that the minimum (d_i, d_e) values of $(R/S\text{-CTA})_2SbCl_5$ are (0.8103, 1.6105) and (0.8095, 1.6096), respectively, which are shorter than the minimum (d_i, d_e) values of (0.9562, 1.7954) in $TMCP_2SbCl_5$. It is obvious that the contact between *R*/*S*-CTA cations is stronger than that of TMCP cations, which greatly increases the motion barrier of cations. The results indicate that there is an O–H···Cl hydrogen bonds interaction force between organic cations and $[SbCl_5]^{2-}$ inorganic anions, and it play an important role in increasing the T_c.

Plastic phase transition analysis

Structural changes are often accompanied by changes in thermal properties, and DSC measurements of $TMCP_2SbCl_5$ and $(R/S\text{-CTA})_2SbCl_5$ are carried out at a rate of 20 K min^{-1} in the

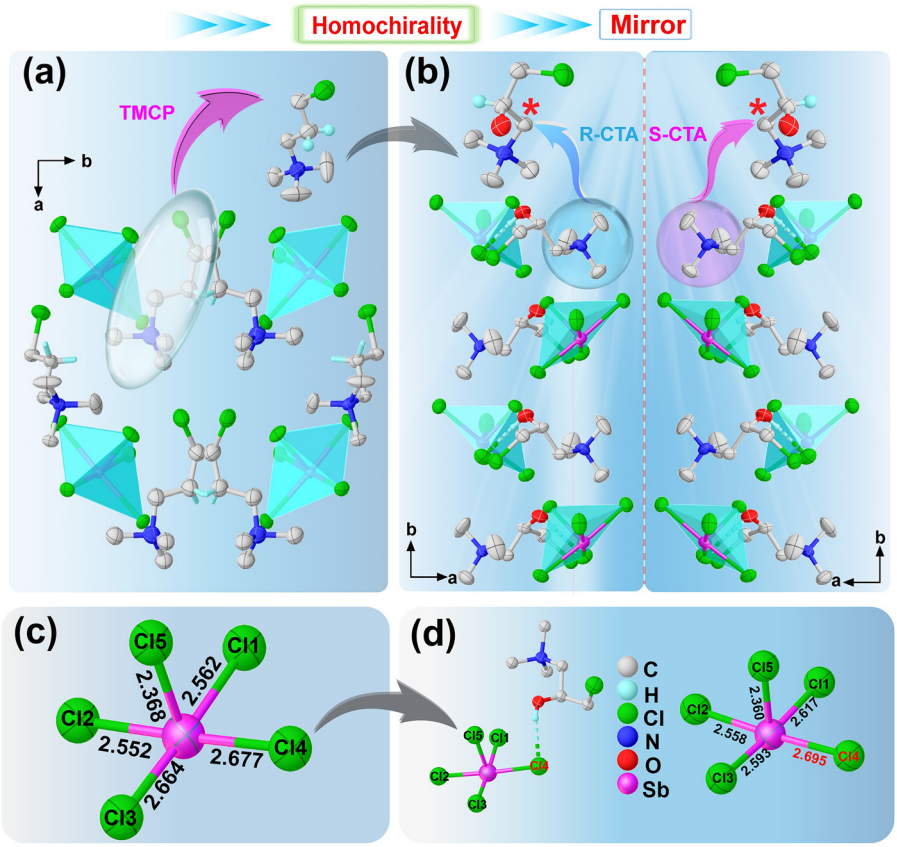

Fig. 1 Packing view along the *c*-axis of the crystal structure of $TMCP_2SbCl_5$ (a) and $(R/S\text{-CTA})_2SbCl_5$ (b). Geometry of the $[SbCl_5]^{2-}$ pyramid of $TMCP_2SbCl_5$ (c). Hydrogen-bonding interactions between the inorganic skeleton and *R*-CAT cations, and geometry of the $[SbCl_5]^{2-}$ pyramid of $(R\text{-CTA})_2SbCl_5$ (d).

temperature range of 320 K to 430 K. Fig. 3a and b show that $TMCP_2SbCl_5$ and $(R/S\text{-CTA})_2SbCl_5$ exhibit a pair of endothermic/exothermic peaks during heating and cooling, indicating that $TMCP_2SbCl_5$ and $(R/S\text{-CTA})_2SbCl_5$ undergo reversible phase transitions at 390 K and 410 K, respectively. There is a significant difference in the phase transition between compounds $TMCP_2SbCl_5$ and $(R/S\text{-CTA})_2SbCl_5$, which is due to the introduction of hydroxyl groups that generate hydrogen bonds, increasing the energy barrier of $(R/S\text{-CTA})_2SbCl_5$ and the T_c of $(R/S\text{-CTA})_2SbCl_5$ by 20 K. Through the homochiral strategy, the T_c of $(R/S\text{-CTA})_2SbCl_5$ is at a higher level in the lead-free ferroelastic semiconductor[32,33,40,48–58] (Fig. 3c). In addition, the thermal hysteresis of 20 K and 45 K reveal the first-order phase transition type of $TMCP_2SbCl_5$ and $(R/S\text{-CTA})_2SbCl_5$. The entropy changes (ΔS) of $TMCP_2SbCl_5$ and $(R/S\text{-CTA})_2SbCl_5$ are 1.83, 68.75, and 66.09 J mol^{-1} K^{-1}, respectively. At the same time, the entropy change during phase transition is greater than that during melting, indicating that $(R/S\text{-CTA})_2SbCl_5$ exhibits the characteristic of plastic phase transition (Fig. 3g and Fig. S3 ESI†). The larger ΔS indicates that $(R/S\text{-CTA})_2SbCl_5$ shows a high degree of disorder in the plastic phase, and their phase transition type should be ordered–disordered ferroelastic phase transition. The dielectric constant, as a temperature dependent function, usually exhibits significant abrupt changes near the T_c. During the heating process, the real part (ε') of the dielectric constant of $TMCP_2SbCl_5$ and $(R/S\text{-CTA})_2SbCl_5$ exhibits a stepped mutation near 390 K and 410 K, respectively. During cooling operation, the ε' exhibits the same trend of change at 340 K and 365 K, which is consistent with the results of DSC (Fig. 3c–e). It is worth noting that near the phase

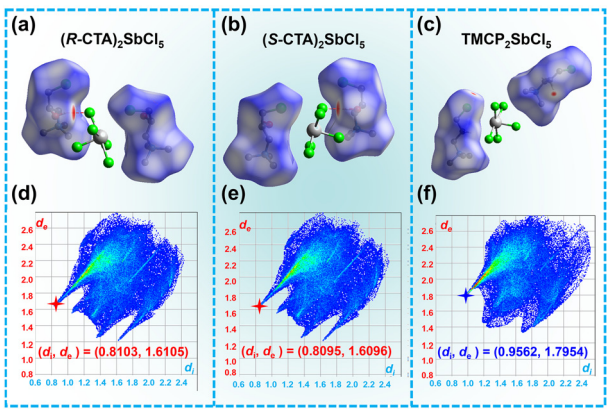

Fig. 2 Hirshfeld d_{norm} surfaces of $(R\text{-CTA})_2SbCl_5$ (a), $(S\text{-CTA})_2SbCl_5$ (b), and $(TMCP)_2SbCl_5$ (c). 2D fingerprint plots of *R*/*S*-CTA cations (d and e) and the TMCP cation (f).

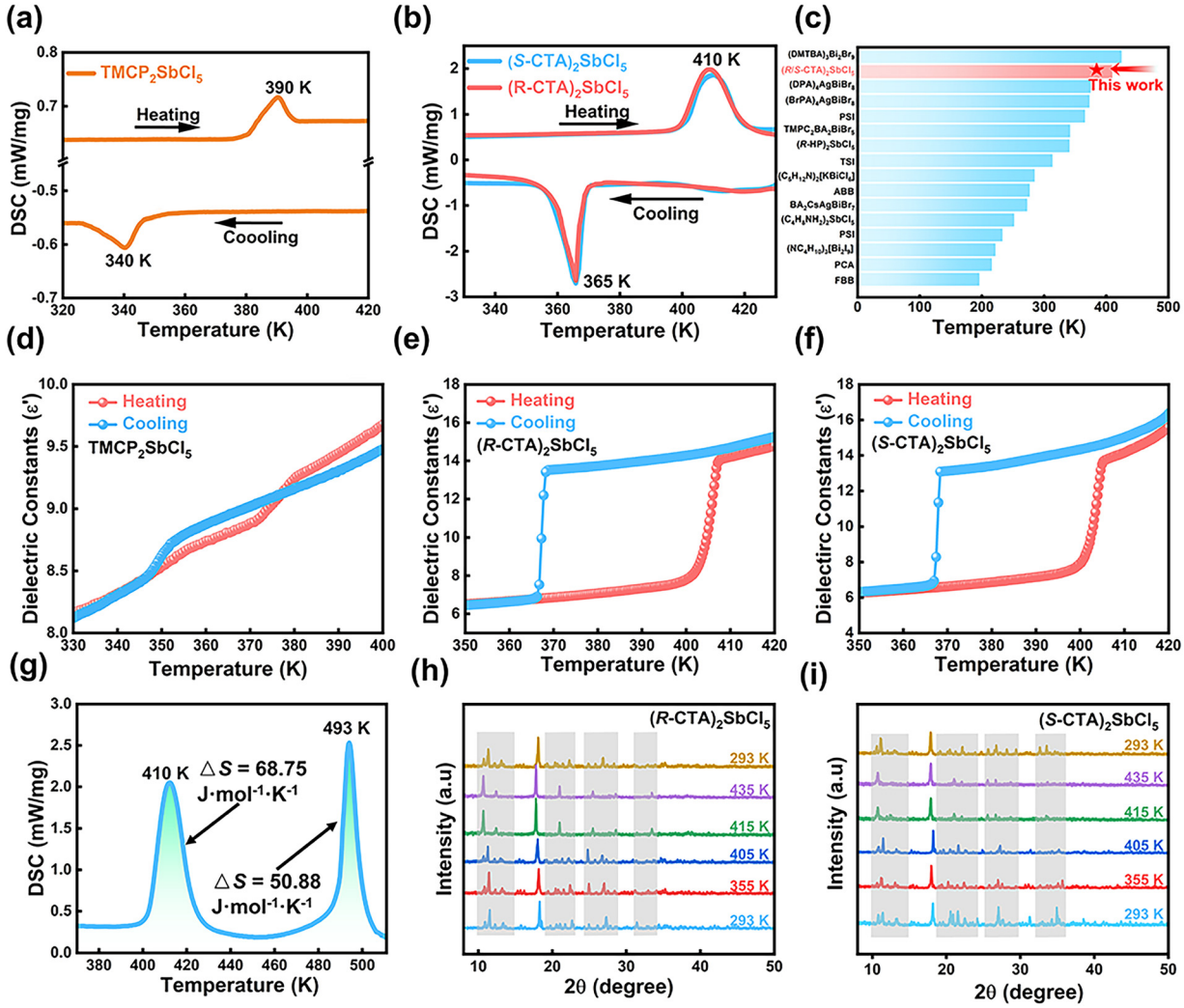

Fig. 3 DSC curves of $TMCP_2SbCl_5$ (a) and $(R/S\text{-CTA})_2SbCl_5$ (b). Reported T_c of lead-free ferroelastic semiconductor materials (c). FBB, PCA $(NC_4H_{10})_3[Bi_2I_9]$, PSI, $(C_4H_8NH_2)SbCl_5$, $BA_2CsAgBiBr_7$, ABB, $(C_5H_{12}N)_2[KBiCl_6]$, TSI, $(R\text{-HP})_2SbCl_5$, $(BrPA)_4AgBiBr_8$, $(DPA)_4AgBiBr_8$, and $(DMTB)_3ABiBr_9$. Dielectric curves of $TMCP_2SbCl_5$ (d), $(R\text{-CTA})_2SbCl_5$ (e), and $(S\text{-CTA})_2SbCl_5$ (f). The entropy change of the plastic phase transition surpasses that of melting. (g). Variable-temperature PXRD patterns of $(R\text{-CTA})_2SbCl_5$ (h) and $(S\text{-CTA})_2SbCl_5$ (i).

transition point, the ε' value undergoes nearly twice the change, which is consistent with the larger entropy change of $(R/S\text{-CTA})_2SbCl_5$. $TMCP_2SbCl_5$ exhibits insignificant dielectric anomalies near the phase transition temperature, indicating slight structural changes in the vicinity of the phase transition.

Variable-temperature PXRD

Due to the fact that $(R/S\text{-CTA})_2SbCl_5$ is a plastic crystal above T_c, its accurate high-temperature structure cannot be obtained. In order to further obtain high temperature structural data for $(R/S\text{-CTA})_2SbCl_5$, variable-temperature powder diffraction was used to measure the PXRD data of $(R/S\text{-CTA})_2SbCl_5$. When the temperature is 300 K, the PXRD data of $(R/S\text{-CTA})_2SbCl_5$ well match the data obtained from crystal structure simulation, which proves that $(R/S\text{-CTA})_2SbCl_5$ has good crystallinity and purity (Fig. S1, ESI†). As shown in Fig. 3h and i, the $(R/S\text{-CTA})_2SbCl_5$ powder diffraction plot did not change below T_c, indicating that the sample has good thermal stability. After reaching the T_c, the PXRD pattern of $(R/S\text{-CTA})_2SbCl_5$ shows significant changes. As $(R/S\text{-CTA})_2SbCl_5$ is a pair of enantiomers with the same phase transition type, only $(R\text{-CTA})_2SbCl_5$ will be analyzed in detail. In the range of 10–18°, a series of peaks disappear, but new diffraction peaks appear at 11°. From 20–30°, new diffraction peaks appear at 22° and 26°, but all other peaks in this range disappear. In the high angle region bigger than 30°, only a new diffraction peak appears at 34°, and the rest of the diffraction peaks remain unchanged. When cooling to room temperature, the PXRD pattern of $(R\text{-CTA})_2SbCl_5$ corresponds to the original pattern, indicating good thermal reversibility of the sample. After the phase transition point, the number of diffraction peaks of $(R\text{-CTA})_2SbCl_5$ significantly decreases, indicating that $(R\text{-CTA})_2SbCl_5$ has high symmetry after the phase transition. Through Pawley refinement and simulation of the PXRD pattern at 435 K, it was found that the structure of $(R\text{-CTA})_2SbCl_5$ above the T_c belongs to the 422 point group of the tetragonal crystal system (Fig. S5, ESI†).

Nonlinear optical properties

Nonlinear materials with the SHG effect are often used to detect non-centrosymmetric crystals, as the SHG effect occurs in non-centrosymmetric crystals. The introduction of chirality lead $(R/S\text{-CTA})_2SbCl_5$ to crystallize in the non-centrosymmetric space group $P2_12_12_1$. As shown in Fig. 4c and d, at 273 K, the SHG signal of $(R/S\text{-CTA})_2SbCl_5$ is very active. During the heating process, $(R/S\text{-CTA})_2SbCl_5$ still has SHG intensity and can maintain a stable SHG intensity at temperatures below T_c, which is defined as the SHG-active state. When the temperature reaches near the T_c, the SHG intensity rapidly decreases to zero, which can be regarded as an inactive state of SHG. During the cooling process, the SHG intensity can be restored to its original state. The SHG intensity of $(R/S\text{-CTA})_2SbCl_5$ switches back and forth between the SHG-active and SHG-inactive states, indicating that $(R/S\text{-CTA})_2SbCl_5$ is a potential nonlinear switching material. Although $(R/S\text{-CTA})_2SbCl_5$ is still in the chiral space group at high temperatures, according to the Kleinman rule, the chiral space group 422 622 432 does not exhibit SHG-activity, which is very consistent with the simulation results of variable temperature PXRD (Fig. S5a and b, ESI†). At the same time, the SHG intensity of $(R/S\text{-CTA})_2SbCl_5$ was measured in the low-temperature phase, which is approximately 0.6 and 0.5 times (Fig. S6, ESI†) that of the typical second-order nonlinear material KDP (KH_2PO_4). It is noteworthy that the SHG intensities of $(R\text{-CTA})_2SbCl_5$ and $(S\text{-CTA})_2SbCl_5$ are not equal, which may be due to the size-dependent SHG intensity. Therefore, the SHG intensities of $(R/S\text{-CTA})_2SbCl_5$ at different particle sizes were measured for phase matching analysis, and Fig. 4c shows that the SHG intensity of the $(R/S\text{-CTA})_2SbCl_5$ gradually increases with increasing particle size, which indicates that $(R/S\text{-CTA})_2SbCl_5$ have excellent SHG phase matching characteristics.

Semiconductors

Due to the inherent semiconductor properties of stibium-based compounds, the band structure of $(R/S\text{-CTA})_2SbCl_5$ crystals was studied at room temperature through solid-state UV-visible spectroscopy and theoretical calculations. The UV visible absorption spectrum of $(R/S\text{-CTA})_2SbCl_5$ shows strong absorption at the beginning of the band edge at 400 nm (Fig. 4c). Since $(R\text{-CTA})_2SbCl_5$ and $(S\text{-CTA})_2SbCl_5$ are a pair of enantiomers, $(R\text{-CTA})_2SbCl_5$ is chosen for analysis. Using the *Tauc* plot $(\alpha h\nu)^{1/n} = A(h\nu - E_g)$ (where α, h, ν, and A represent the absorption coefficient, Planck constant, light frequency, and proportionality constant, respectively, and $n = 2$ represents the indirect bandgap and $n = 1/2$ represents the direct bandgap), the characteristics of the indirect bandgap semiconductor can be obtained (Fig. 4d, illustration). In order to gain a deeper understanding of the electronic structure of $(R\text{-CTA})_2SbCl_5$ (Fig. 4e), we also calculated the band structure, with the conduction band minimum (CBM) and valence band maximum (VBM) located at the vectors of different Brillouin regions. From this, we can conclude that $(R\text{-CTA})_2SbCl_5$ is an indirect bandgap semiconductor, which is very consistent with the experimental phenomenon. It is worth noting that the energy distribution of the VBM is quite flat, indicating that the electronic states of

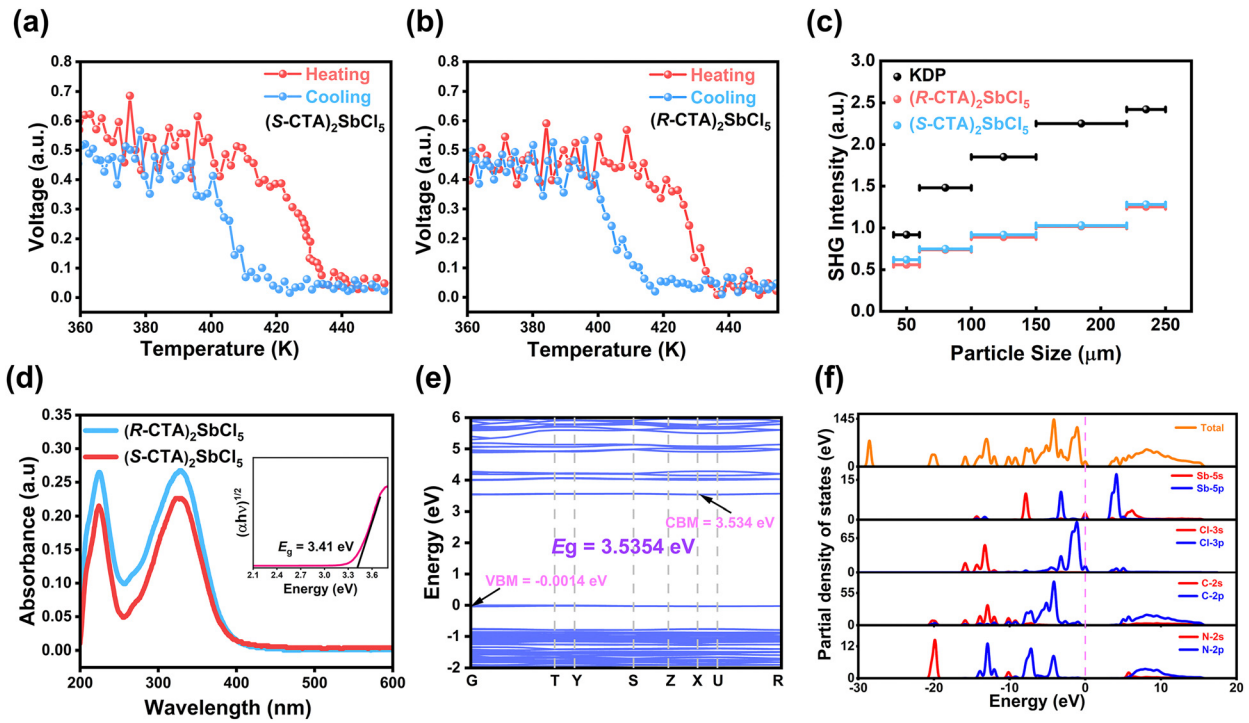

Fig. 4 The changes of SHG intensity of $(R\text{-CTA})_2SbCl_5$ (a) and $(S\text{-CTA})_2SbCl_5$ (b) during heating and cooling. The SHG intensity of $(R/S\text{-CTA})_2SbCl_5$ and KDP with different particle sizes at room temperature (c). UV-vis absorption spectra of $(R/S\text{-CTA})_2SbCl_5$. The inset shows the Tauc plot for $(R\text{-CTA})_2SbCl_5$ (d). The energy-band structure (e) and the partial density of states (PDOS) (f) of $(R\text{-CTA})_2SbCl_5$.

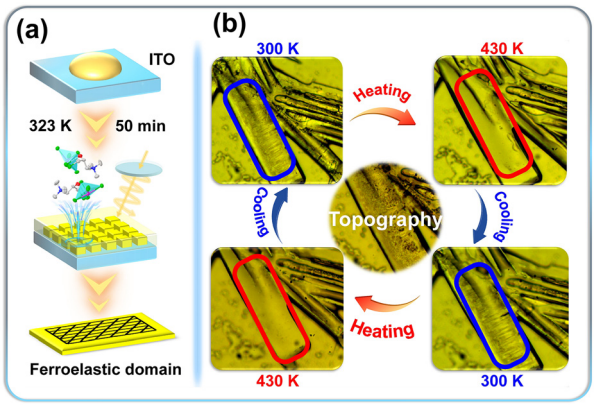

Fig. 5 Preparation process of $(R\text{-CTA})_2SbCl_5$ thin films (a). Evolution of ferroelastic domains for $(R\text{-CTA})_2SbCl_5$ (b).

$(R\text{-CTA})_2SbCl_5$ are highly localized due to the limited charge carriers.[25] In addition, energy bands can be allocated based on partial density of states (PDOS) (Fig. 4f). From the PDOS perspective, the energy band at the top of the VBM originates from the unbonded state of Cl-3p, while the energy band at the bottom of the CBM mainly comes from the unoccupied Sb-5p orbital. Obviously, the bandgap of the material is determined by the inorganic $[SbCl_5]^{2-}$ skeleton.

Ferroelasticity

Based on the simulation results of variable-temperature PXRD and the measurement results of variable-temperature SHG, it can be inferred that $(R/S\text{-CTA})_2SbCl_5$ belongs to the 422 point in the high-temperature phase, therefore $(R/S\text{-CTA})_2SbCl_5$ undergoes the 422F222 type phase transition. According to the Auzi rule,[59] it undergoes one of the 94 types of ferroelastic phase transitions. As shown in Fig. 5a, films were prepared by dropwise addition of a mixed solution of DMSO (2 mL) and $(R\text{-CTA})_2SbCl_5$ (30 mg) onto ITO glass and then heated at 323 K for 50 min. $(R\text{-CTA})_2SbCl_5$ was used as a representative to observe its ferroelastic domain transition using a polarizing microscope (Fig. 5b). In the initial state (300 K), $(R\text{-CTA})_2SbCl_5$ belongs to the ferroelastic phase, and the thin film crystal of $(R\text{-CTA})_2SbCl_5$ has a single domain state. When the temperature rises to the T_c (430 K), $(R\text{-CTA})_2SbCl_5$ transitions to the paraelastic phase, and the sample transforms into a highly symmetric tetragonal phase. The single domain state disappears when viewed under a polarizing microscope. When the temperature cools to room temperature, the sample exhibits striped domain structures again. The significant changes in ferroelastic domains with temperature evolution demonstrate the ferroelasticity of $(R\text{-CTA})_2SbCl_5$. At the same time, the samples are measured in two heating and cooling cycles, and the results showed that the domain structure of the sample switched between appearance and disappearance, indicating that the domain structure of $(R\text{-CTA})_2SbCl_5$ has outstanding reversibility and stability.

Conclusions

In summary, the high-T_c lead-free ferroelastic semiconductor $(R/S\text{-CTA})_2SbCl_5$ with a direct bandgap of 3.41 eV has been successfully synthesized using the H/OH-substitution-induced homochiral strategy. They undergo plastic phase transition with a large entropy gain at 410 K (ΔS = 68.75 J mol^{-1} K^{-1} much higher than its melting enthalpy). Due to the introduction of chirality, they crystallize in the non-centrosymmetric space group $P2_12_12_1$ exhibiting good SHG signals, while also increasing the T_c of $(R/S\text{-CTA})_2SbCl_5$ by 20 K. Variable-temperature PXRD and SHG data indicate that $(R/S\text{-CTA})_2SbCl_5$ undergoes a 422F222 type ferroelastic phase transition at 410 K. With the change of external temperature, the ferroelastic domain structure of $(R/S\text{-CTA})_2SbCl_5$ undergoes significant changes. This work, which provides an approach for obtaining high-T_c lead-free ferroelastic semiconductors, is a powerful motivation for the realization of multifunctional materials related to chirality.

Author contributions

B.-W. Deng performed the synthesis and analysis of the compounds; Z.-P. Rao and M.-J. Shen checked the writing; K.-W. Liang designed part of the experimental figures; Z.-X. Zhang, Y. Zhang and D.-W. Fu guided the synthesis and writing; Zhu and other authors analyzed the experimental data and discussed the conclusions.

Conflicts of interest

There are no conflicts to declare.

Acknowledgements

The authors thank the support of the Jiangsu Key Laboratory for Science and Applications of Molecular Ferroelectrics, and Southeast University.

References

1 C. C. Fan, X. B. Han, B. D. Liang, C. Shi, L. P. Miao, C. Y. Chai, C. D. Liu, Q. Ye and W. Zhang, *Adv. Mater.*, 2022, **34**, e2204119.
2 J. Harada, M. Takehisa, Y. Kawamura, H. Takahashi and Y. Takahashi, *Adv. Electron. Mater.*, 2022, **8**, 2101415.
3 M. M. Lun, H. F. Ni, Z. X. Zhang, J. Y. Li, Q. Q. Jia, Y. Zhang, Y. Zhang and D. W. Fu, *Angew. Chem., Int. Ed.*, 2024, **63**, e202313590.
4 J. Y. Li, T. Zhang, M. M. Lun, Y. Zhang, L. Z. Chen and D. W. Fu, *Small*, 2023, **19**, e2301364.
5 J. X. Gao, W. Y. Zhang, Z. G. Wu, Y. X. Zheng and D. W. Fu, *J. Am. Chem. Soc.*, 2020, **142**, 4756–4761.
6 Y. Ai, P. F. Li, M. J. Yang, Y. Q. Xu, M. Z. Li and R. G. Xiong, *Chem. Sci.*, 2022, **13**, 748–753.
7 B. D. Liang, C. C. Fan, C. D. Liu, C. Y. Chai, X. B. Han and W. Zhang, *Nat. Commun.*, 2022, **13**, 6599.

8 L. P. Miao, N. Ding, N. Wang, C. Shi, H. Y. Ye, L. Li, Y. F. Yao, S. Dong and Y. Zhang, *Nat. Mater.*, 2022, **21**, 1158–1164.
9 Y. Zhang, X.-J. Song, Z.-X. Zhang, D.-W. Fu and R.-G. Xiong, *Matter*, 2020, **2**, 697–710.
10 Y. Xie, Y. Ai, Y. L. Zeng, W. H. He, X. Q. Huang, D. W. Fu, J. X. Gao, X. G. Chen and Y. Y. Tang, *J. Am. Chem. Soc.*, 2020, **142**, 12486–12492.
11 X. J. Song, T. Zhang, Z. X. Gu, Z. X. Zhang, D. W. Fu, X. G. Chen, H. Y. Zhang and R. G. Xiong, *J. Am. Chem. Soc.*, 2021, **143**, 5091–5098.
12 H. Cho, S.-H. Jeong, M.-H. Park, Y.-H. Kim, C. Wolf, C.-L. Lee, J. H. Heo, A. Sadhanala, N. Myoung, S. Yoo, S. H. Im, R. H. Friend and T.-W. Lee, *Science*, 2015, **350**, 1222–1225.
13 D. Yang, G. Zhang, R. Lai, Y. Cheng, Y. Lian, M. Rao, D. Huo, D. Lan, B. Zhao and D. Di, *Nat. Commun.*, 2021, **12**, 4295.
14 P. P. Shi, Y. Y. Tang, P. F. Li, W. Q. Liao, Z. X. Wang, Q. Ye and R. G. Xiong, *Chem. Soc. Rev.*, 2016, **45**, 3811–3827.
15 H. Y. Zhang, C. L. Hu, Z. B. Hu, J. G. Mao, Y. Song and R. G. Xiong, *J. Am. Chem. Soc.*, 2020, **142**, 3240–3245.
16 Y.-Y. Zhang, J.-Q. Luo, Y. Han, W.-Y. Zhang, Y. Zhang, H.-F. Lu and D.-W. Fu, *Chin. Chem. Lett.*, 2024, DOI: **10.1016/j.cclet.2024.109530**.
17 Y.-Y. Chen, C.-H. Gao, T. Yang, W.-J. Li, H.-J. Xu and Z.-H. Sun, *Chin. J. Struct. Chem.*, 2022, **41**, 2204001.
18 J. Q. Luo, M. M. Lun, Q. Q. Jia, Z. J. Wang, H. F. Lu, Y. Zhang and D. W. Fu, *Chin. J. Chem.*, 2024, **42**, 1706–1712.
19 W. Li, Z. Wang, F. Deschler, S. Gao, R. H. Friend and A. K. Cheetham, *Nat. Rev. Mater.*, 2017, **2**, 16099.
20 X. Xiao, W. Li, Y. Fang, Y. Liu, Y. Shao, S. Yang, J. Zhao, X. Dai, R. Zia and J. Huang, *Nat. Commun.*, 2020, **11**, 2215.
21 Y. Yalcinkaya, I. M. Hermes, T. Seewald, K. Amann-Winkel, L. Veith, L. Schmidt-Mende and S. A. L. Weber, *Adv. Energy Mater.*, 2022, **12**, 2202442.
22 E. Strelcov, Q. F. Dong, T. Li, J. Chae, Y. C. Shao, Y. H. Deng, A. Gruverman, J. S. Huang and A. Centrone, *Adv. Sci.*, 2017, **3**, e1602165.
23 Y. L. Zeng, X. Q. Huang, C. R. Huang, H. Zhang, F. Wang and Z. X. Wang, *Angew. Chem., Int. Ed.*, 2021, **60**, 10730–10735.
24 X. Q. Huang, H. Zhang, F. Wang, T. Gan, Z. K. Xu and Z. X. Wang, *J. Phys. Chem. Lett.*, 2021, **12**, 5221–5227.
25 M. M. Lun, C. Y. Su, J. Li, Q. Q. Jia, H. F. Lu, D. W. Fu, Y. Zhang and Z. X. Zhang, *Small*, 2023, **19**, e2303127.
26 Y. He, Z. Chen, X. Chen, X.-M. Zhang and D. Fu, *Mater. Chem. Front.*, 2022, **6**, 1292–1300.
27 G. Teri, Q.-Q. Jia, Q. Guo, Y. Zhang and D.-W. Fu, *Sci. China Mater.*, 2023, **66**, 3687–3695.
28 C. Y. Su, Z. X. Zhang, J. Yao, M. Chen, P. Z. Huang, Y. Zhang, D. W. Fu and L. Y. Xie, *Chin. Chem. Lett.*, 2023, **34**, 107442.
29 M. Rok, M. Moskwa, J. Hetmańczyk, Ł. Hetmańczyk and G. Bator, *CrystEngComm*, 2022, **24**, 4932–4939.
30 H. Peng, Q. Liu, Y. H. Liu, Y. Z. Lu and W. Q. Liao, *Chin. Chem. Lett.*, 2023, **34**, 107980.
31 K. Ding, H. Ye, C. Su, Y. A. Xiong, G. Du, Y. M. You, Z. X. Zhang, S. Dong, Y. Zhang and D. W. Fu, *Nat. Commun.*, 2023, **14**, 2863.
32 Q. Liu, H. Peng, J. C. Qi, Y. Z. Lu, S. J. Yang and W. Q. Liao, *Chem. Commun.*, 2023, **59**, 1793–1796.
33 Z. Yue, F. Wu, X. Li, Y. Liu, J. Luo and X. Liu, *Sci. China Mater.*, 2023, **66**, 3977–3983.
34 M.-M. Lun, T. Zhang, C.-Y. Su, J. Li, Z.-X. Zhang, D.-W. Fu and H.-F. Lu, *Mater. Chem. Front.*, 2022, **6**, 1929–1937.
35 M. Rok, B. Zarychta, J. Trojan-Piegza, A. Bil, A. Piecha-Bisiorek, J. K. Zaręba, W. Medycki and R. Jakubas, *J. Mater. Chem. C*, 2022, **10**, 3036–3047.
36 M.-Z. Li, Z.-H. Chen, S.-Q. Hu, J.-S. Zhou, L.-Y. Ji and X.-G. Chen, *J. Mater. Chem. C*, 2023, **11**, 15952–15958.
37 Y. Zeng, J. Liu, L. Zhou, X. Deng, W. Yang, X. Yan, Y. Luo, X. Zhu, X. Huang, X. Song and Y. Tang, *Chin. Chem. Lett.*, 2023, **34**, 108127.
38 K. Xu, Z. Zhou, J. Men, Q. Zhou and Q. Ye, *Inorg. Chem. Front.*, 2023, **10**, 5064–5070.
39 Y. J. Cao, L. Zhou, P. P. Shi, Q. Ye and D. W. Fu, *Chem. Commun.*, 2019, **55**, 8418–8421.
40 J. Mu, K. Xu, L. He, Y. Xu, T.-J. Yin, J.-T. Men and Q. Ye, *Chem. Commun.*, 2023, **59**, 1209–1212.
41 H. Peng, Z. K. Xu, Y. Du, P. F. Li, Z. X. Wang, R. G. Xiong and W. Q. Liao, *Angew. Chem., Int. Ed.*, 2023, **62**, e202306732.
42 Y. L. Zeng, Y. Ai, S. Y. Tang, X. J. Song, X. G. Chen, Y. Y. Tang, Z. X. Zhang, Y. M. You, R. G. Xiong and H. Y. Zhang, *J. Am. Chem. Soc.*, 2022, **144**, 19559–19566.
43 J.-Q. Luo, Q.-Q. Jia, G. Teri, M.-M. Lun, Z.-J. Wang, Z.-X. Zhang, Y. Zhang and D.-W. Fu, *ACS Mater. Lett.*, 2023, 452–460, DOI: **10.1021/acsmaterialslett.3c01458**.
44 R. G. Xiong, S. Q. Lu, Z. X. Zhang, H. Cheng, P. F. Li and W. Q. Liao, *Angew. Chem., Int. Ed.*, 2020, **59**, 9574–9578.
45 H. Ye, W.-H. Hu, W.-J. Xu, Y. Zeng, X.-X. Chen, R.-K. Huang, W.-X. Zhang and X.-M. Chen, *APL Mater.*, 2021, **9**, 031102.
46 D. W. Fu, J. X. Gao, W. H. He, X. Q. Huang, Y. H. Liu and Y. Ai, *Angew. Chem., Int. Ed.*, 2020, **59**, 17477–17481.
47 Z. B. Hu, C. F. Wang, T. T. Sha, C. Shi, L. Ye, H. Y. Ye, Y. Song, Y. M. You and Y. Zhang, *Small Methods*, 2022, **6**, e2200421.
48 Q. R. Meng, W. J. Xu, W. H. Hu, H. Ye, X. X. Chen, W. Yuan, W. X. Zhang and X. M. Chen, *Chem. Commun.*, 2021, **57**, 6292–6295.
49 C. Y. Su, Y. F. Yao, Z. X. Zhang, Y. Wang, M. Chen, P. Z. Huang, Y. Zhang, W. C. Qiao and D. W. Fu, *Chem. Sci.*, 2022, **13**, 4794–4800.
50 X. Liu, Z. Xu, P. Long, Y. Yao, C. Ji, L. Li, Z. Sun, M. Hong and J. Luo, *Chem. Mater.*, 2020, **32**, 8965–8970.
51 K. Mencel, V. Kinzhybalo, R. Jakubas, J. K. Zaręba, P. Szklarz, P. Durlak, M. Drozd and A. Piecha-Bisiorek, *Chem. Mater.*, 2021, **33**, 8591–8601.

52 M. Wojciechowska, A. Gągor, A. Piecha-Bisiorek, R. Jakubas, A. Ciżman, J. K. Zaręba, M. Nyk, P. Zieliński, W. Medycki and A. Bil, *Chem. Mater.*, 2018, **30**, 4597–4608.
53 Z.-X. Zhang, C.-Y. Su, J. Li, X.-J. Song, D.-W. Fu and Y. Zhang, *Chem. Mater.*, 2021, **33**, 5790–5799.
54 K. Mencel, P. Starynowicz, M. Siczek, A. Piecha-Bisiorek, R. Jakubas and W. Medycki, *Dalton Trans.*, 2019, **48**, 14829–14838.
55 P. Szklarz, A. Gagor, R. Jakubas, W. Medycki and G. Bator, *Dalton Trans.*, 2023, **52**, 11981–11991.
56 P. Szklarz, R. Jakubas, W. Medycki, A. Gagor, J. Cichos, M. Karbowiak and G. Bator, *Dalton Trans.*, 2022, **51**, 1850–1860.
57 M. Ksiądzyna, A. Gągor, A. Piecha-Bisiorek, A. Ciżman, W. Medycki and R. Jakubas, *J. Mater. Chem. C*, 2019, **7**, 10360–10370.
58 M. Rowinska, A. Piecha-Bisiorek, W. Medycki, P. Durlak, R. Jakubas and A. Gagor, *Molecules*, 2023, **28**, 3894.
59 K. Aizu, *Phys. Rev. B: Solid State*, 1970, **2**, 754–772.